Article

Boundary-induced excitation of higher-order hyperbolic phonon polaritons

Na Chen[1,2,9], Hanchao Teng[1,2,3,9], Hai Hu[1,2] ✉, F. Javier García de Abajo[4,5], Rainer Hillenbrand[6,7,8] ✉ & Qing Dai[3] ✉

Higher-order hyperbolic phonon polaritons (HoHPhPs), arising from photon–phonon coupling under geometric confinement and resonance conditions, exhibit larger wavevectors, field confinement and tunability compared with fundamental hyperbolic phonon polariton (HPhP) modes, making them promising for compact nanophotonic devices. However, their excitation remains challenging due to stringent momentum compensation requirements, leaving their properties and applications largely unexplored. Here we overcome this challenge by introducing a boundary-induced scattering mechanism that facilitates the efficient stepwise excitation of HoHPhPs. By creating a high-contrast dielectric environment with a gold–air hybrid substrate, we achieve substantial momentum compensation through scattering at the gold edge. Our approach is validated by theoretical analysis using dyadic Green's function theory, demonstrating more than a sixfold increase in the excitation efficiency of HoHPhPs compared with conventional antenna-launching of HPhP. Experimentally, we observe HoHPhPs in α-MoO_3 layers with a propagation distance of up to 15.2 μm and report a pseudo-birefringence effect with an ultrahigh equivalent birefringence ranging from 17.6 to 41.8. Thus, different polariton orders are spatially separated by their propagation direction without altering their polarization state. Our work introduces a novel strategy for the efficient excitation of HoHPhPs and establishes them as a versatile platform for nanophotonic applications such as mode routing in nanocircuits.

Polaritons are quasiparticles resulting from the strong coupling of photons with excitations that possess an electric dipole moment[1–5]. These quasiparticles can confine free-space light to nanoscale dimensions[6–12], and thus offer great potential for deep subwavelength photonic devices[13–18]. Particularly for higher-order hyperbolic phonon polaritons (HoHPhPs)[19,20], they originate from the geometric confinement and resonance enhancement of photon–phonon coupling in nanostructures or multilayer interfaces. These HoHPhPs exhibit richer dispersion relations, stronger field confinement and more flexible tunability, leading to enhanced light–matter interactions and even the potential for optical nonlinearity[21]. Such properties promise important applications in compact nanophotonic circuits and highly sensitive sensors. However, the excitation of these modes remains challengeing, leaving their properties, control and potential applications largely unexplored.

The excitation of polaritons critically depends on achieving wavevector (momentum) matching, particularly because their wavevectors are much larger than those of free-space light. Direct excitation of polaritons has been widely explored using a variety of techniques, including far- and near-field optical methods, as well as electrical approaches[22]. Real-space near-field imaging of polaritons based on scattering-type scanning near-field optical microscopy

A full list of affiliations appears at the end of the paper. ✉e-mail: huh@nanoctr.cn; r.hillenbrand@nanogune.eu; daiqing@sjtu.edu.cn

(s-SNOM) techniques[23–25], where polaritons are launched by the near-field probe itself[6,7], metal antennas[26–28] or edges[29,30], have gained increasing popularity for covering the wide spectral range between visible and terahertz frequencies[31–36], ultrahigh spatial, energy and temporal resolution[37–40], multiphysics integration[41–45], and precise phase-resolved mapping[46,47]. However, these methods are constrained by providing only single-step momentum compensation, preventing the stepwise excitation of polaritons across multiple orders[48]. This limitation is particularly pronounced for hyperbolic phonon polaritons (HPhPs)[49], which require excitation over a much broader range of wavevectors to simultaneously excite multiple higher order modes[50,51].

In this work, we introduce two-step excitation of HoHPhPs through boundary-induced scattering, which combines antenna-mediated launching of HPhPs with subsequent boundary-induced scattering to generate HoHPhPs. By carefully designing a high-contrast dielectric environment using a gold (Au)–air hybrid substrate, we demonstrate that fundamental phonon polaritons (FPhPs) in α-phase molybdenum trioxide (α-MoO_3) layers can be efficiently scattered at the sharp edge of a single-crystalline Au layer, providing substantial momentum compensation. This enables the excitation of HoHPhPs with momenta far exceeding those of the incident FPhPs. We support this wavevector transition process between different polariton orders through calculations based on dyadic Green's function, showing more than a sixfold increase in the excitation efficiency of HoHPhPs compared with conventional single-step excitation. Furthermore, the low-loss properties of the HPhPs in suspended α-MoO_3 layers permit the observation of HoHPhPs with a propagation distance of up to 15.2 μm. Leveraging this high-quality propagation, we show that scattering of HPhPs at the Au edge can lead to pseudo-birefringence. This phenomenon is characterized by a spatial separation of propagation directions across different polariton orders, with an ultrahigh equivalent birefringence (Δn) ranging from 17.6 to 41.8 at varying illumination frequencies. Two-step excitation and spatial separation of HoHPhPs may have important implications for applications including the design of highly efficient polariton launchers and multimode photonic devices in nanocircuits for mode-division multiplexing and demultiplexing.

Figure 1a illustrates the concept of two-step HoHPhP excitation. A Au–air hybrid substrate is designed to achieve the boundary-induced excitation of HoHPhPs in a layer placed on top of the substrate. In the Au-supported layer, the coupling between the HPhPs with their mirror image gives rise to image polaritons with larger wavevectors and amplitudes compared to those in the suspended layer[52,53]. When FPhPs (k_{in}^{F}) in the layer on the Au substrate, which are excited by a local source (orange dot in Fig. 1a), scatter at the Au edge (high dielectric constant substrate), they convert into multiple HPhP orders in the suspended layer (low dielectric constant substrate). This includes new FPhPs (k_{out}^{F}) and HoHPhPs ($k_{out}^{H^1}$ and $k_{out}^{H^2}$) in the suspended region. Unlike conventional transmission from a dense to a sparse medium, the wavevector of the outcoupled HoHPhPs can exceed the wavevector of the incident FPhPs due to momentum compensation, which arises from the scattering of the incident polaritons at the boundary.

To demonstrate two-step excitation of HoHPhPs, we study HPhPs supported by a thin layer of α-MoO_3 within its second Reststrahlen band (816–972 cm^{-1}), particularly along the [100] crystal axis[54–56]. Figure 1b presents the IFCs of HPhPs in an α-MoO_3 layer, with the left panel showing those for the layer supported by a Au substrate and the right panel showing those for the suspended layer. To directly compare the wavevector magnitudes of different HPhP orders generated by scattering at the Au edge, we schematically illustrate the HPhP wavevector conversion process (Fig. 1c). In particular, the conversion of FPhPs in the α-MoO_3 layer supported by a Au substrate to those in the suspended α-MoO_3 film results in a reduction of the wavevector ($k_{in}^{F} > k_{out}^{F}$). Conversely, conversion to HoHPhPs necessitates momentum compensation ($k_{out}^{H^2} > k_{out}^{H^1} > k_{in}^{F}$). This requires that the compensatory wavevectors (δk) rapidly increase with the increasing HPhP order, owing to the growing wavevector magnitude.

To quantify the efficiency of two-step excitation of HoHPhPs, we use dyadic Green's function theory (Fig. 1d,e and Supplementary Note 1)[57–59]. The excitation efficiency $\langle \alpha_{G/S}^{m} \rangle_t$ can be expressed as

$$\langle \alpha_{G/S}^{m} \rangle_t = \left\langle \alpha_{G}^{F} T_{m1} e^{ik_z^S z_d} \delta\left(k - k_S^m\right) \right\rangle_t, \quad (1)$$

where T_{m1} denotes the transition efficiency from FPhPs in the α-MoO_3 layer on the Au substrate to the m-order HPhPs in the suspended layer. The subscripts S, G and G/S refer to suspended layer, the layer on the Au substrate and the layer on the Au–air hybrid substrate, respectively. $\alpha_G^F = \frac{ik_G^1 \alpha_{ant}}{2\varepsilon} r^p(k_G^1 \cos(\theta), k_G^1 \sin(\theta)) e^{ik_G^1 z_0}$ represents the efficiency of the primary (corresponding to a single-step) excitation of FPhPs on the Au substrate with a point dipole located $z_0 = 30$ nm above the surface. k_G^1 represents the in-plane wavevectors of the FPhPs and θ denotes the angle between the in-plane wavevector direction and the [100] of the α-MoO_3 layer. The superscripts F and H denote the fundamental and higher-order polaritons, respectively. z_d denotes the height where the polariton fields are evaluated. k_S^m and k_z^S represent the in-plane and out-plane wavevectors in the suspended α-MoO_3 layer (Supplementary Note 1).

For single-step HPhP excitation with the dipole, the excitation efficiency ratio of first-order HPhPs to FPhPs is $|a_S^{H^1}|/|a_S^F| = 1/7$ for the suspended α-MoO_3 layer (Fig. 1e and Supplementary Fig. 1b,c) and $|a_G^{H^1}|/|a_G^F| = 2/13$ for the α-MoO_3 layer on a Au substrate (Supplementary Fig. 1d,e). This ratio is strongly enhanced for two-step excitation of HPhPs utilizing the hybrid Au-air substrate (Fig. 1d and Supplementary Fig. 1f,g), since the FPhPs on the Au substrate share the same mode distribution as the first-order HPhPs in the suspended α-MoO_3 region[53,60]. Therefore, most of the FPhPs in α-MoO_3 on Au can be transferred to HoHPhPs in the suspended α-MoO_3 layer after being scattered at the Au-air boundary, that is, the Au edge (Supplementary Fig. 2). This conversion can be calculated through both wavevector and modal matching at the Au-air boundary (Supplementary Note 1). Compared with the traditional impedance-matching approach[61,62], this method enables a more accurate description of the conversion between different polaritons. We obtain an excitation efficiency ratio of first-order HPhPs to FPhPs of $|a_{G/S}^{H_{out}^1}|/|a_{G/S}^{F_{out}}| = 5/6$ in the suspended α-MoO_3 region, corresponding to an enhancement of the excitation efficiency ratio of approximately sixfold compared with single-step HoHPhP excitation on the suspended α-MoO_3 layer (Fig. 1e). Note that the excitation efficiency decreases as the dipole–surface distance increases (Supplementary Fig. 3). We extract the excitation efficiency based on the same criterion in all calculations (Supplementary Note 1).

The mechanism of boundary-induced excitation of HoHPhPs can be directly visualized in real space using full-wave numerical simulations (Fig. 1d). HoHPhPs exhibit substantially shorter wavelengths compared with FPhPs, enabling their identification in spatial electric field distributions. In particular, the effectiveness of boundary-induced excitation of HoHPhPs strongly depends on the boundary sharpness such as the curvature of the Au edge (Supplementary Fig. 4). As the boundary sharpness decreases, the HoHPhP amplitude in the suspended α-MoO_3 region decreases. This further supports that boundary scattering compensates for the wavevector mismatch between HPhPs on the two sides of the Au–air boundary. A systematic evaluation of various hybrid substrates (Au–air, SiO_2–air, Si–air, CaF_2–air and h-BN–air) reveals that the Au–air hybrid substrate exhibits the highest excitation efficiency ratio (Supplementary Fig. 5).

To observe experimentally the boundary-induced excitation of HoHPhPs, we designed and fabricated a specific polariton device (Fig. 2a). Nanofabrication techniques were used to pattern a SiO_2 on Si substrate with square holes of 246-nm depth. A subsequent aligned

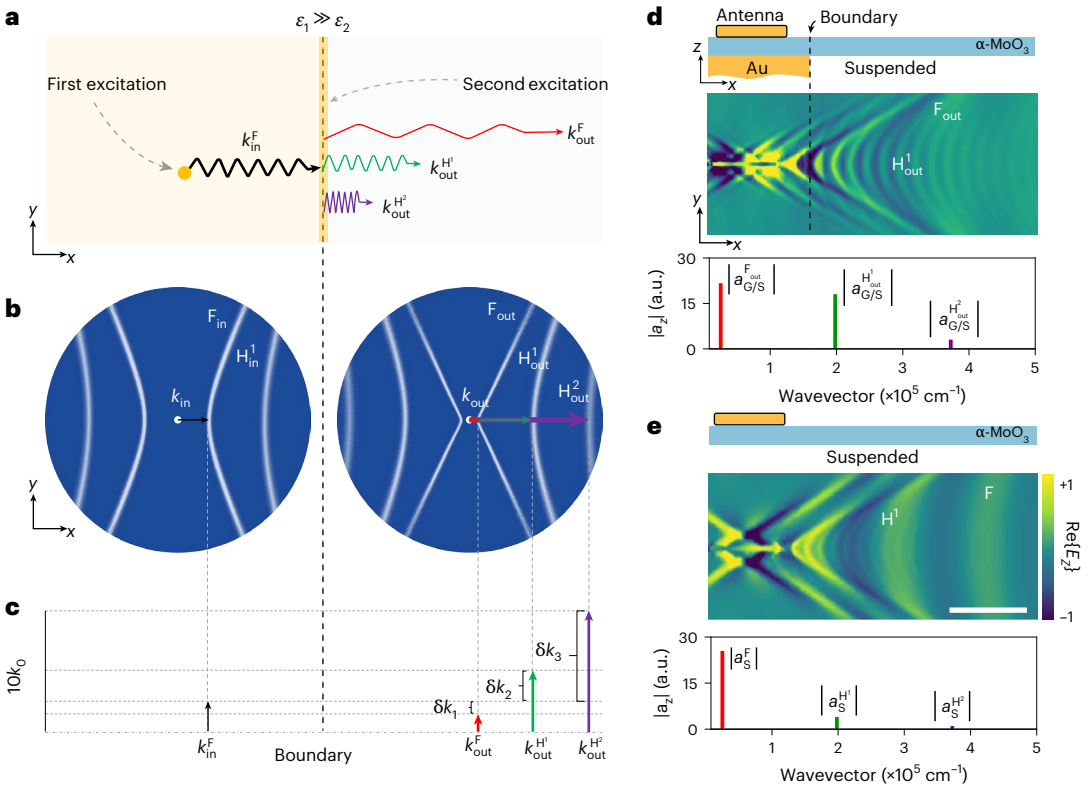

Fig. 1 | Two-step excitation of HoHPhPs. a, Schematic of the boundary-induced excitation of HoHPhPs in a thin layer on a substrate comprising a large (left) and small (right) dielectric permittivity. The FPhPs on the left side are initially excited by a launcher (first excitation) and act as an incident polariton, propagating towards the dielectric boundary of the substrate (dashed vertical line). Upon polariton scattering at the boundary (second excitation), momentum compensation is achieved, leading to the excitation of HoHPhPs in the suspended layer on the right side. **b**, Isofrequency contours (IFCs) of polaritons in α-MoO_3 on Au (left) and in suspended α-MoO_3 (right), which are obtained from transmission matrix calculations. The arrows on the left (k_{in}^{F}) and right (k_{out}^{F}, $k_{out}^{H^1}$, $k_{out}^{H^2}$) sides indicate the wavevectors of the incident and transmitted polaritons at the Au–air boundary, analogous to **a**. **c**, Quantitative comparison of different wavevectors. δk indicates the mismatch between k_{in} and k_{out}. **d**, Top: Numerically simulated spatial distribution of the electric field Re{E_z} of HPhPs in an α-MoO_3 layer on a Au–air hybrid substrate. Bottom: Two-step excitation efficiency for the generation of polaritons of different orders. **e**, Analogue to **d**, but for single-step HPhP exciation on suspended α-MoO_3. $|a_{G/S}^{F_{out}}|$, $|a_{G/S}^{H^1_{out}}|$ and $|a_{G/S}^{H^2_{out}}|$ in **d** denote the two-step excitation efficiencies for output FPhPs, first-order HPhPs and second-order HPhPs on a Au–air hybrid substrate, respectively. $|a_S^F|$, $|a_S^{H^1}|$ and $|a_S^{H^2}|$ in **e** are the single-step excitation efficiencies for the suspended α-MoO_3 layer. The schematics in **d** and **e** present cross-sectional views of the structures. Scale bar, 3 µm. The thickness of α-MoO_3 is 300 nm and the illumination frequency is 900 cm^{-1} in all panels. F_{in}, F_{out}, H_{out}^1, and H_{out}^2 denote incident FPhPs, output FPhPs, output first-order HPhPs and output second-order HPhPs, respectively.

transfer process was used to deposit a high-quality Au flake on one side of the substrate, forming a well-defined Au–air boundary. To minimize scattering losses arising from substrate roughness, we utilized single-crystal Au flakes, renowned for their atomically smooth surfaces and inherent sharp edges[63]. Next, a 380-nm-thick α-MoO_3 was transferred onto the substrate, bridging the Au flake and the square holes, thereby forming a suspended region with a suspension height of approximately 246 nm. Au antennas, serving as the initial source for exciting HPhPs in α-MoO_3 on the Au substrate, were fabricated on top of the α-MoO_3 layer at a distance of 2 µm from the Au–air boundary. An optical image of the sample is presented in Fig. 2b. The transmitted HPhPs were visualized using s-SNOM. Experimental details are provided in the Methods and Supplementary Figs. 6 and 7).

Under illumination with a focused *p*-polarized mid-infrared laser beam, Au antennas excite propagating HPhPs in the α-MoO_3 layer that is supported by the Au substrate (Fig. 2c). Upon reaching the Au–air boundary, the abrupt change in substrate permittivity induces strong scattering of the HPhPs. In the suspended part of the α-MoO_3 flake, we thus observe both FPhPs (F_{out}) and first-order HPhPs (H_{out}^1). The FPhPs feature a relatively large wavelength of ~3,000 nm. By contrast, the HoHPhPs exhibit a much smaller wavelength of ~580 nm, which agrees well with simulations (Supplementary Fig. 8). In addition to the wavelength difference, FPhPs and HoHPhPs can also be distinguished by the tilt of their interference fringes relative to each other, which reflects the different opening angles of their IFCs.

For comparison, Fig. 2e shows a near-field amplitude image of antenna-excited HPhPs in a fully suspended α-MoO_3 flake, whereas Supplementary Fig. 9a shows the corresponding near-field image for an α-MoO_3 flake fully supported by a Au substrate. Because the stringent wavevector-matching conditions for HoHPhP excitation are not satisfied, only FPhPs are observed in both cases. Note that the tip also launches HPhPs. However, being volume modes, they are barely reflected by the antenna. The observed fringes therefore mainly originate from antenna-launched HPhPs, with the spacing between adjacent fringes corresponding to one wavelength. Spatial Fourier transform analysis of near-field amplitude profiles from the suspended α-MoO_3 region (Fig. 2d) reveals both FPhPs (F_{out}) and first-order HPhPs (H_{out}^1). By contrast, Fourier transform analysis of near-field amplitude profiles from the fully suspended α-MoO_3 flake (Fig. 2f) and the α-MoO_3 flake fully supported by a Au substrate (Supplementary Fig. 9b) reveals only FPhPs.

Numerical simulations show that HoHPhPs are weakly affected by the finite suspension height of the α-MoO_3 flake due to their extremely high field confinement (Supplementary Fig. 10). As shown

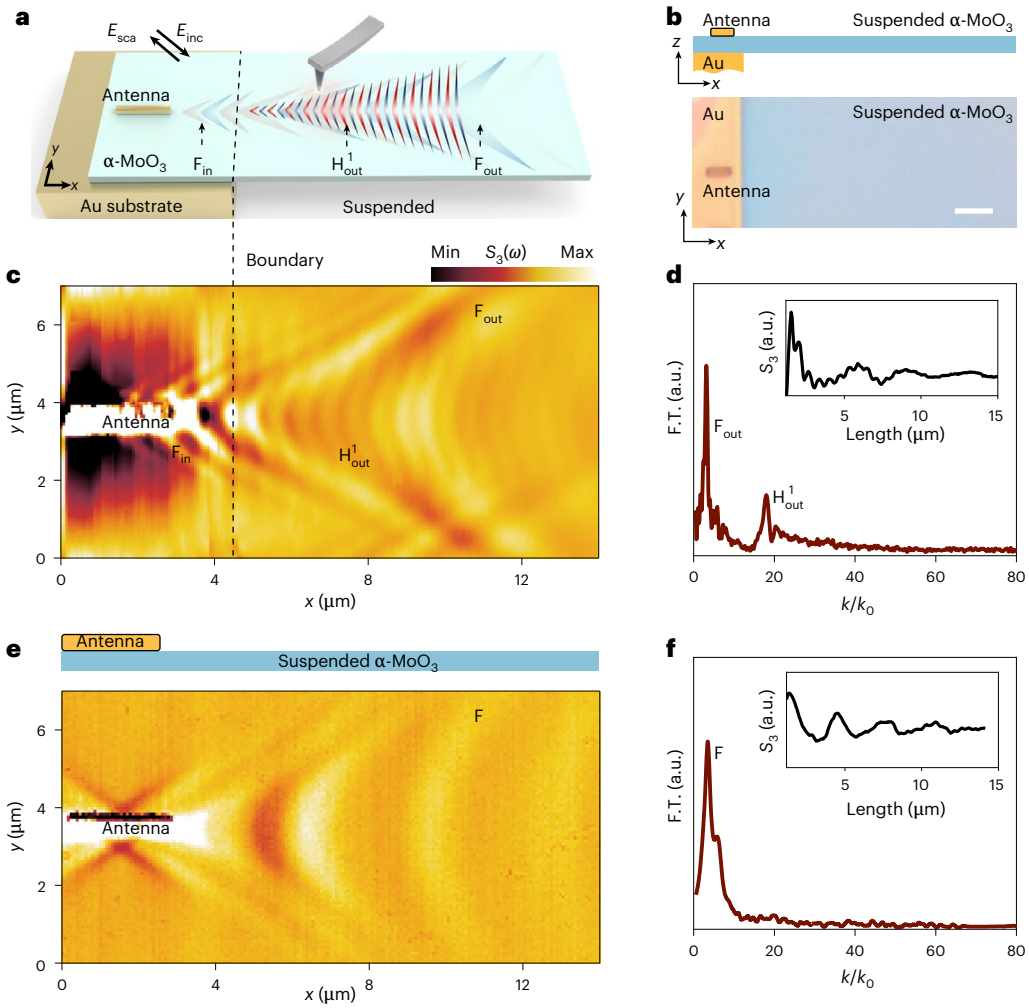

Fig. 2 | Real-space imaging of boundary-induced HoHPhP excitation using s-SNOM. a, Schematic of the experiment. A Au substrate featuring a square trench supports a partially suspended exfoliated α-MoO_3 flake. A Au antenna is located on the part of the α-MoO_3 flake that is supported by the Au substrate and illuminated by a mid-infrared laser beam to excite HPhPs in the α-MoO_3 flake. The near field of the antenna-launched propagating polaritons is scattered by the atomic force microscopy tip and recorded with an infrared detector. **b**, Sketch and optical image of the sample used for two-step excitation of HoHPhPs. The Au substrate consists of a thin, single-crystalline Au flake. Scale bar, 5 μm. **c**,**d**, Experimentally measured near-field amplitude (S_3) image of HPhPs in α-MoO_3 on a Au–air hybrid substrate at $\omega = 900\ cm^{-1}$ (**c**) and its Fourier transform (F.T.) spectrum revealing FPhPs and HoHPhPs (**d**). The inset shows a near-field line profile extracted from **c**. **e**,**f**, Control experiment analogue to **c** (**e**) and **d** (**f**) where the antenna is placed on the suspended α-MoO_3 flake.

in Supplementary Fig. 10d, at a suspension height of 246 nm, the wavelength of HoHPhPs is 492 nm, which is consistent with that of the infinite suspension region.

The efficient excitation of HoHPhPs through boundary-induced scattering provides an excellent platform for investigating their key properties. To quantitatively assess the wavelength confinement and propagation characteristics within the suspended region, we analysed line profiles extracted from the experimental near-field image in Fig. 2c (Supplementary Fig. 12 shows additional profiles at different excitation frequencies). Filtering of the line profiles enables the separation of the different HPhP orders (Fig. 3a).

We investigated the dispersion of the HPhPs by performing measurements of their wavevector at various frequencies within the hyperbolic Reststrahlen band. These wavevectors are subsequently mapped onto the theoretically calculated dispersion (pseudo-colour plot) presented in Fig. 3b. As expected, both F_{out} and H^1_{out} polaritons exhibit a decrease in wavelength with increasing frequency (Supplementary Fig. 13). The green and red solid dots represent the experimental data for FPhPs (F_{out}) and first-order HPhPs (H^1_{out}) extracted from the near-field profiles shown in Supplementary Figs. 11–13, showing good agreement with the theoretical dispersion calculations (pseudo-colour plot in Fig. 3b).

The excitation of higher-order modes can be further enhanced when a Au strip is placed on top of the α-MoO_3 layer above the Au-air hybrid substrate boundary, forming a Au–α-MoO_3–Au sandwich structure (Supplementary Fig. 14). This allows for the excitation of second-order HPhPs (H^2_{out}) in the suspended α-MoO_3 region (Fig. 3b, black circles). The wavelength of the H^2_{out} HPhPs is approximately 1/50 of the incident light wavelength in free space and 1/4 of FPhPs in the α-MoO_3 layer on the Au substrate (Supplementary Fig. 14).

Monocrystalline Au flakes provide an atomically flat, low-loss substrate for HPhPs[52], whereas in the suspended α-MoO_3 layer substrate-induced HPhP losses are maximally reduced. This combination practically eliminates roughness-mediated HPhP scattering and HPhP dissipation in the subtrate, respectively. Consequently, our structure enables long-distance propagation of HoHPhPs, which can be quantified by a figure of merit (FOM) and propagation distance L, defined as $FOM = \mathrm{Re}(q_p)/\mathrm{Im}(q_p)$ and $L = 1/(2\mathrm{Im}(q_p))$, respectively[27].

The first-order HPhP profile shown in Fig. 3c is well fitted with a model that describes HPhPs as damped plane waves. From this fitting

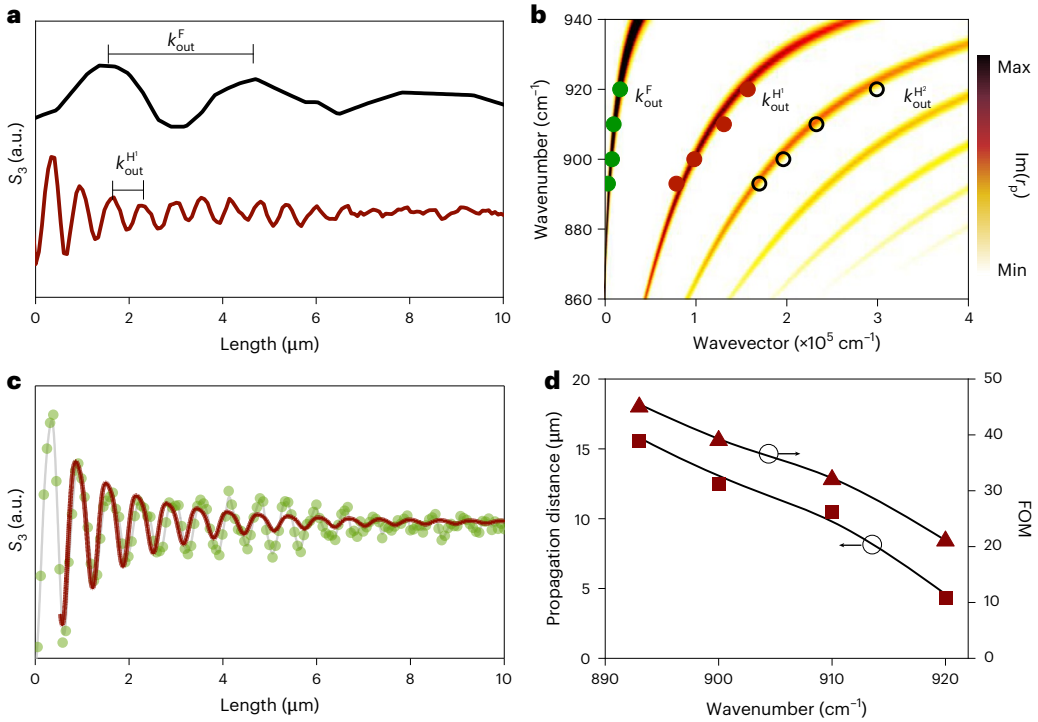

Fig. 3 | Dispersion and loss analysis of HoHPhPs. a, Experimental near-field amplitude profiles of fundamental and first-order HPhPs on the suspended α-MoO_3 region, extracted from Fig. 2c. Output FPhPs (F_{out}, black profile) and first-order HPhPs (H^1_{out}, red profile) were separated by spatial filtering. **b**, Theoretically calculated dispersion (pseudo-colour plot) of HPhPs in a suspended α-MoO_3 layer of 380 nm thickness. Dots are experimental data extracted from near-field images shown in Supplementary Fig. 11. Circles are obtained from simulated near-field images. **c**, Loss analysis of first-order HPhPs. Red curve shows the fit of the experimental near-field amplitude profile (dots; same data as red curve in **a**). **d**, FOM (triangles) and propagation distance (squares) of first-order HPhPs (H^1_{out}) in the suspended α-MoO_3 region as a function of illuminating frequency. The solid curves are guides to the eyes.

we determine the FOM of first-order HPhPs at 900 cm^{-1}, reaching a notable value of FOM ≈ 39, which corresponds to a propagation distance $L \approx 12.5$ μm. Damping is primarily attributed to HPhP scattering at acoustic phonons and impurities (such as isotopic impurities or oxygen vacancy defects). Figure 3d depicts the dependence of the FOM and propagation distance of HoHPhPs in the suspended α-MoO_3 region as a function of frequency (Supplementary Fig. 12). We find that the FOM can reach up to 45 at an illuminating frequency of 893 cm^{-1} ($L \approx 15.2$ μm). As the frequency increases, the mode confinement and group velocity increase, which leads to a gradual decrease in the FOM and propagation distance. Future measurements at low temperatures may reduce phonon–phonon scattering, potentially leading to a notable enhancement in the FOM and propagation distance of HoHPhPs[64,65].

The low-loss propagation of HoHPhPs enables us to investigate their unique refraction properties. According to Snell's law, refraction requires the conservation of the tangential wavevector component[66–68]. For that reason, when HPhPs impinge on the Au–air boundary at an oblique angle, they refract along two distinct directions, a phenomenon we refer to as pseudo-birefringence. This effect arises from the differing opening angles of the IFCs of the different HPhP orders (Fig. 4a).

In Fig. 4a, we illustrate how the incident polaritons with a wavevector $\mathbf{k}^F_{in}$ refract at the Au-air boundary into the suspended α-MoO_3 region. The wavevectors of the refracted polaritons are indicated by $\mathbf{k}^F_{out}$ and $\mathbf{k}^{H^1}_{out}$, whereas the Poynting vectors (indicating the polaritonic energy flow) are indicated by $\mathbf{S}^F_{in}$, $\mathbf{S}^F_{out}$ and $\mathbf{S}^{H^1}_{out}$. By varying the angle of incidence, the direction of the wavevector of the outgoing FPhPs and HoHPhPs, as well as the angle between these wavevectors, can be controlled (Supplementary Fig. 15).

To experimentally demonstrate pseudo-birefringence involving different HPhP orders, a rectangular Au patch with a side length of 3 μm (Fig. 4b) is used to excite plane-wave HPhPs in α-MoO_3 on Au, which are characterized by the wavevector $\mathbf{k}^F_{in}$. Because the polariton wavevector component parallel to the Au-air boundary is conserved, pseudo-birefringence occurs when the HPhPs refract at this boundary (Fig. 4c,d). On the suspended α-MoO_3 region, we thus observe two distinct modes propagating in different directions. They correspond to FPhPs and first-order HPhPs. To determine the direction of **S** for the different polariton orders, we extracted multiple near-field profiles along various propagation directions. By comparing these profiles, we identify the direction with the longest propagation length, which corresponds to the direction of **S** (ref. 69). By contrast, **k** is perpendicular to the polariton fringes (Supplementary Note 2 and Supplementary Figs. 16 and 17a,b). The directions of the refracted polariton Poynting vector **S** and wavevector **k** agree well with both the numerical simulation (Fig. 4d) and theoretical prediction (Fig. 4a). We note that not only the near fields of the Au patch but also the near fields at the Au-air boundary and the tip apex launch HPhPs, resulting in unwanted interference fringes parallel to the boundary. To isolate the antenna-excited polaritons from the near-field images, we applied a filtering procedure that is described in Supplementary Fig. 18.

We also studied the pseudo-birefringence for different illumination frequencies between 893 cm^{-1} and 918 cm^{-1} (Supplementary Fig. 19). By extracting the wavelengths and refraction angles of the two refracted polaritons' orders at different frequencies, we obtained their dispersion (Supplementary Fig. 20a) and frequency-dependent refraction angles (Fig. 4e and Supplementary Fig. 17c). We find that the refraction angle of both FHPhPs and first-order HPhPs associated with **S** exhibit a strong frequency dependency ($\varphi_S^{F_{out}} \in (0.2°–11.5°)$ and $\varphi_S^{H^1_{out}} \in (40.2°–49.3°)$; Fig. 4e), whereas the refraction angle associated with **k** shows a pronounced frequency response only for FHPhPs ($\varphi_k^{F_{out}} \in (71.3°–81.7°)$) (Supplementary Fig. 17) and is nearly constant for the first-order HPhPs (Supplementary Fig. 16). Our experimentally measured

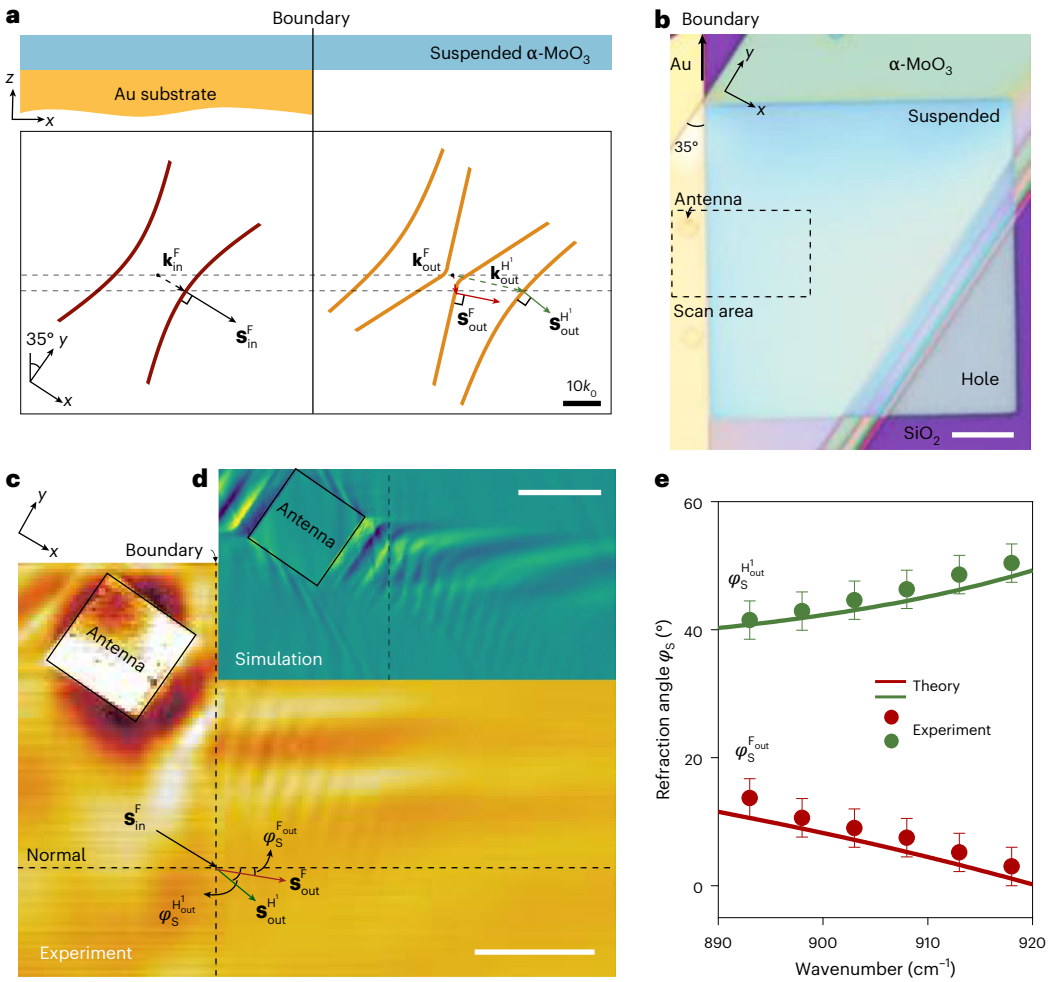

Fig. 4 | Spatial separation of FPhPs and HoHPhPs via pseudo-birefringence. **a**, IFCs of HPhPs in α-MoO_3 on the Au substrate (left) and in suspended α-MoO_3 (right). The [001] crystal orientation is rotated 35° relative to the Au–air boundary. Considering conservation of the polariton wavevector that is parallel to the Au-air boundary, the FPhP ($\mathbf{k}^{F}_{out}$) and first-order HPhP ($\mathbf{k}^{H^1}_{out}$) wavevectors on the suspended α-MoO_3 region are obtained (dashed arrows). The solid arrows $\mathbf{S}^{F}_{in}$, $\mathbf{S}^{F}_{out}$ and $\mathbf{S}^{H^1}_{out}$ are the Poynting vectors, which are normal to the IFCs. The dashed horizontal lines are normal to the Au-air boundary. A cross-section of the device is shown at the top of the panel. **b**, Optical image of a typical device, corresponding to the design in **a**. The dashed rectangle indicates the area where the image shown in **c** was recorded. Scale bar, 10 µm. **c**,**d**, Experimental (S_3) and numerical near-field amplitude images, demonstrating the spatial separation of FPhPs and HoHPhPs when a plane FPhP wave launched by a rectangular Au patch impinges on the Au-air boundary. The thickness of the α-MoO_3 film is 345 nm. The illuminating frequency is $\omega = 893\ cm^{-1}$. Scale bar, 3 µm. $\varphi_S^{F_{out}}$ and $\varphi_S^{H^1_{out}}$ denote the refraction angle of the Poynting vector for FPhPs and first-order HPhPs in suspended α-MoO_3, respectively. The subscript S in φ_S denotes the Poynting vector. **e**, Refraction angle φ_S of the Poynting vector of FPhPs ($\varphi_S^{F_{out}}$) and first-orderHPhPs ($\varphi_S^{H^1_{out}}$) in suspended α-MoO_3 as a function of illuminating frequency. The solid curves show the result of analytical calculations, whereas the dots show data extracted from experimental near-field images. Since the experimental refraction angles φ_S were determined visually, we assign conservative error bars of ±3°.

refraction angles agree well with theoretical calculations (Fig. 4e (solid lines) and Supplementary Fig. 17c).

We note that the pseudo-birefringence phenomenon described in this work is similar to birefringence observed in traditional anisotropic crystals such as calcite and quartz[70]. In contrast, the polarization state of the refracted polaritons is preserved. By evaluating the difference in the effective mode indices of FPhPs and first-order HPhPs (Supplementary Fig. 20b), we find a mode-index contrast of $\Delta n = n_H - n_F = 17.6–41.8$ for illumination frequencies between 893 cm^{-1} and 918 cm^{-1}. This difference is more than one to two orders of magnitude larger than the birefringence typically observed in naturally anisotropy crystals[70]. The pronounced pseudo-birefringence of HPhPs promises new opportunities for the design of novel nanoscale optical devices, including multimode polaritonic devices for mode-division multiplexing and demultiplexing within a bus waveguide. While previous studies have proposed phonon polariton refraction via substrate engineering[71] and phase-change substrates[72], our work introduces boundary-induced HPhP exciation for efficient generation of HoHPhPs and their spatial separation from FPhPs.

In this work, we introduce a two-step excitation mechanism for efficiently generating HoHPhPs. The approach combines initial antenna-mediated launching of HPhPs with subsequent boundary-induced scattering to produce HoHPhPs, resulting in more than a sixfold increase in excitation efficiency compared with single-step excitation. Moreover, exploiting a suspended α-MoO_3 layer minimizes substrate-induced damping, allowing HoHPhPs to propagate over a distance of 15.2 µm with a quality factor of ~45. Leveraging the high-efficiency excitation and long propagation lengths, we observe pseudo-birefringence, in which different polariton orders propagate along distinct directions while preserving their polarization state. This corresponds to an ultrahigh birefringence of 41.8, exceeding that of natural anisotropic crystals by one to two orders of magnitude.

Our findings offer new design strategies for highly efficienent HoHPhP launching and opens new avenues for multimode polaritonic devices for applications including mode-division multiplexing and demultiplexing.

Online content

Any methods, additional references, Nature Portfolio reporting summaries, source data, extended data, supplementary information, acknowledgements, peer review information; details of author contributions and competing interests; and statements of data and code availability are available at https://doi.org/10.1038/s41566-025-01755-5.

References

1. Basov, D., Fogler, M. & García de Abajo, F. J. S. Polaritons in van der Waals materials. *Science* **354**, aag1992 (2016).
2. Low, T. et al. Polaritons in layered two-dimensional materials. *Nat. Mater.* **16**, 182–194 (2017).
3. Zhang, Q. et al. Interface nano-optics with van der Waals polaritons. *Nature* **597**, 187–195 (2021).
4. Galiffi, E. et al. Extreme light confinement and control in low-symmetry phonon-polaritonic crystals. *Nat. Rev. Mater.* **9**, 9–28 (2024).
5. Wu, Y. et al. Manipulating polaritons at the extreme scale in van der Waals materials. *Nat. Rev. Phys.* **4**, 578–594 (2022).
6. Chen, J. et al. Optical nano-imaging of gate-tunable graphene plasmons. *Nature* **487**, 77–81 (2012).
7. Fei, Z. et al. Gate-tuning of graphene plasmons revealed by infrared nano-imaging. *Nature* **487**, 82–85 (2012).
8. Dai, S. et al. Tunable phonon polaritons in atomically thin van der Waals crystals of boron nitride. *Science* **343**, 1125–1129 (2014).
9. Huber, A., Ocelic, N., Kazantsev, D. & Hillenbrand, R. Near-field imaging of mid-infrared surface phonon polariton propagation. *Appl. Phys. Lett.* **87**, 081103 (2005).
10. Orsini, L. et al. Deep subwavelength topological edge state in a hyperbolic medium. *Nat. Nanotechnol.* **19**, 1485–1490 (2024).
11. Woessner, A. et al. Highly confined low-loss plasmons in graphene–boron nitride heterostructures. *Nat. Mater.* **14**, 421–425 (2015).
12. Ocelic, N. & Hillenbrand, R. Subwavelength-scale tailoring of surface phonon polaritons by focused ion-beam implantation. *Nat. Mater.* **3**, 606–609 (2004).
13. Woessner, A. et al. Electrical 2π phase control of infrared light in a 350-nm footprint using graphene plasmons. *Nat. Photon.* **11**, 421–424 (2017).
14. Xiong, L. et al. Photonic crystal for graphene plasmons. *Nat. Commun.* **10**, 4780 (2019).
15. Hu, H. et al. Far-field nanoscale infrared spectroscopy of vibrational fingerprints of molecules with graphene plasmons. *Nat. Commun.* **7**, 12334 (2016).
16. Freitag, M. et al. Photocurrent in graphene harnessed by tunable intrinsic plasmons. *Nat. Commun.* **4**, 1951 (2013).
17. Luo, Y. et al. Electrically switchable anisotropic polariton propagation in a ferroelectric van der Waals semiconductor. *Nat. Nanotechnol.* **18**, 350–356 (2023).
18. Teng, H., Chen, N., Hu, H., García de Abajo, F. J. & Dai, Q. Steering and cloaking of hyperbolic polaritons at deep-subwavelength scales. *Nat. Commun.* **15**, 4463 (2024).
19. Norrman, A., Setälä, T. & Friberg, A. T. Long-range higher-order surface-plasmon polaritons. *Phys. Rev. A* **90**, 053849 (2014).
20. Lu, G. et al. Launching and manipulation of higher-order in-plane hyperbolic phonon polaritons in low-dimensional heterostructures. *Adv. Mater.* **35**, 2300301 (2023).
21. Zhang, Y., Kartashov, Y., Torner, L., Li, Y. & Ferrando, A. Nonlinear higher-order polariton topological insulator. *Opt. Lett.* **45**, 4710–4713 (2020).
22. García de Abajo, F. J. Optical excitations in electron microscopy. *Rev. Mod. Phys.* **82**, 209–275 (2010).
23. Chen, X. et al. Modern scattering-type scanning near-field optical microscopy for advanced material research. *Adv. Mater.* **31**, 1804774 (2019).
24. Keilmann, F. & Hillenbrand, R. Near-field microscopy by elastic light scattering from a tip. *Phys. Eng. Sci.* **362**, 787–805 (2004).
25. Hillenbrand, R., Abate, Y., Liu, M., Chen, X. & Basov, D. Visible-to-THz near-field nanoscopy. *Nat. Rev. Mater.* **10**, 285–310 (2025).
26. Alonso-González, P. et al. Controlling graphene plasmons with resonant metal antennas and spatial conductivity patterns. *Science* **344**, 1369–1373 (2014).
27. Ni, G. et al. Fundamental limits to graphene plasmonics. *Nature* **557**, 530–533 (2018).
28. Pons-Valencia, P. et al. Launching of hyperbolic phonon-polaritons in h-BN slabs by resonant metal plasmonic antennas. *Nat. Commun.* **10**, 3242 (2019).
29. Dai, S. et al. Efficiency of launching highly confined polaritons by infrared light incident on a hyperbolic material. *Nano Lett.* **17**, 5285–5290 (2017).
30. Huth, F. et al. Resonant antenna probes for tip-enhanced infrared near-field microscopy. *Nano Lett.* **13**, 1065–1072 (2013).
31. Chen, S. et al. Real-space observation of ultraconfined in-plane anisotropic acoustic terahertz plasmon polaritons. *Nat. Mater.* **22**, 860–866 (2023).
32. Bechtel, H. A., Johnson, S. C., Khatib, O., Muller, E. A. & Raschke, M. B. Synchrotron infrared nano-spectroscopy and -imaging. *Nat. Commun.* **75**, 100493 (2020).
33. Mayer, R. A. et al. Paratellurite nanowires as a versatile material for THz phonon polaritons. *ACS Photon.* **11**, 4323–4333 (2024).
34. Xu, R. et al. Highly confined epsilon-near-zero and surface phonon polaritons in $SrTiO_3$ membranes. *Nat. Commun.* **15**, 4743 (2024).
35. Kehr, S. C., Döring, J., Gensch, M., Helm, M. & Eng, L. M. FEL-based near-field infrared to THz nanoscopy. *Synchrotron Radiat. News* **30**, 31–35 (2017).
36. Álvarez-Cuervo, J. et al. Unidirectional ray polaritons in twisted asymmetric stacks. *Nat. Commun.* **15**, 9042 (2024).
37. Huth, F. et al. Nano-FTIR absorption spectroscopy of molecular fingerprints at 20 nm spatial resolution. *Nano Lett.* **12**, 3973–3978 (2012).
38. Mastel, S. et al. Understanding the image contrast of material boundaries in IR nanoscopy reaching 5 nm spatial resolution. *ACS Photon.* **5**, 3372–3378 (2018).
39. Sternbach, A. et al. Programmable hyperbolic polaritons in van der Waals semiconductors. *Science* **371**, 617–620 (2021).
40. Nishida, J. et al. Ultrafast infrared nano-imaging of far-from-equilibrium carrier and vibrational dynamics. *Nat. Commun.* **13**, 1083 (2022).
41. Wehmeier, L. et al. Landau-phonon polaritons in Dirac heterostructures. *Sci. Adv.* **10**, eadp3487 (2024).
42. Alonso-González, P. et al. Acoustic terahertz graphene plasmons revealed by photocurrent nanoscopy. *Nat. Nanotechnol.* **12**, 31–35 (2017).
43. Xiong, L. et al. Polaritonic vortices with a half-integer charge. *Nano Lett.* **21**, 9256–9261 (2021).
44. Schnell, M. et al. Real-space mapping of the chiral near-field distributions in spiral antennas and planar metasurfaces. *Nano Lett.* **16**, 663–670 (2016).
45. Virmani, D. et al. Amplitude-and phase-resolved infrared nanoimaging and nanospectroscopy of polaritons in a liquid environment. *Nano Lett.* **21**, 1360–1367 (2021).
46. Schnell, M. et al. Controlling the near-field oscillations of loaded plasmonic nanoantennas. *Nat. Photon.* **3**, 287–291 (2009).

47. Schnell, M., Garcia-Etxarri, A., Alkorta, J., Aizpurua, J. & Hillenbrand, R. Phase-resolved mapping of the near-field vector and polarization state in nanoscale antenna gaps. *Nano Lett.* **10**, 3524–3528 (2010).
48. Shi, Z. et al. Amplitude-and phase-resolved nanospectral imaging of phonon polaritons in hexagonal boron nitride. *ACS Photon.* **2**, 790–796 (2015).
49. Li, P. et al. Infrared hyperbolic metasurface based on nanostructured van der Waals materials. *Science* **359**, 892–896 (2018).
50. Ma, Y., Zhong, G., Dai, Z. & Ou, Q. In-plane hyperbolic phonon polaritons: materials, properties, and nanophotonic devices. *npj Nanophoton.* **1**, 25 (2024).
51. Wang, H. et al. Planar hyperbolic polaritons in 2D van der Waals materials. *Nat. Commun.* **15**, 69 (2024).
52. Menabde, S. G. et al. Near-field probing of image phonon-polaritons in hexagonal boron nitride on gold crystals. *Sci. Adv.* **8**, eabn0627 (2022).
53. Lee, I.-H. et al. Image polaritons in boron nitride for extreme polariton confinement with low losses. *Nat. Commun.* **11**, 3649 (2020).
54. Ma, W. et al. In-plane anisotropic and ultra-low-loss polaritons in a natural van der Waals crystal. *Nature* **562**, 557–562 (2018).
55. Zheng, Z. et al. A mid-infrared biaxial hyperbolic van der Waals crystal. *Sci. Adv.* **5**, eaav8690 (2019).
56. Hu, H. et al. Doping-driven topological polaritons in graphene/α-MoO_3 heterostructures. *Nat. Nanotechnol.* **17**, 940–946 (2022).
57. Abdullah, S., Dias, E. J., Krpenský, J., Mkhitaryan, V. & García de Abajo, F. J. Toward complete optical coupling to confined surface polaritons. *ACS Photon.* **11**, 2183–2193 (2024).
58. Nikitin, A. Y., Garcia-Vidal, F. J. & Martin-Moreno, L. Analytical expressions for the electromagnetic dyadic Green's function in graphene and thin layers. *IEEE J. Sel. Topics Quantum Electron.* **19**, 4600611 (2012).
59. Virmani, D., Maciel-Escudero, C., Hillenbrand, R. & Schnell, M. Experimental verification of field-enhanced molecular vibrational scattering at single infrared antennas. *Nat. Commun.* **15**, 6760 (2024).
60. Menabde, S. G., Heiden, J. T., Cox, J. D., Mortensen, N. A. & Jang, M. S. Image polaritons in van der Waals crystals. *Nanophotonics* **11**, 2433–2452 (2022).
61. Nikitin, A. Y., Brucoli, G., García-Vidal, F. & Martín-Moreno, L. Scattering of surface plasmon polaritons by impedance barriers: dependence on angle of incidence. *Phys. Rev. B* **77**, 195441 (2008).
62. Kang, J.-H. et al. Goos-Hänchen shift and even–odd peak oscillations in edge-reflections of surface polaritons in atomically thin crystals. *Nano Lett.* **17**, 1768–1774 (2017).
63. Guo, Z. et al. Facile synthesis of micrometer-sized gold nanoplates through an aniline-assisted route in ethylene glycol solution. *Colloids Surf. A Physicochem. Eng. Asp.* **278**, 33–38 (2006).
64. Voronin, K. V., Álvarez-Pérez, G., Lanza, C., Alonso-González, P. & Nikitin, A. Y. Fundamentals of polaritons in strongly anisotropic thin crystal layers. *ACS Photon.* **11**, 550–560 (2024).
65. Ni, G. et al. Long-lived phonon polaritons in hyperbolic materials. *Nano Lett.* **21**, 5767–5773 (2021).
66. Zhang, T., Zheng, C., Chen, Z. N. & Qiu, C.-W. Negative reflection and negative refraction in biaxial van der Waals materials. *Nano Lett.* **22**, 5607–5614 (2022).
67. Hu, H. et al. Gate-tunable negative refraction of mid-infrared polaritons. *Science* **379**, 558–561 (2023).
68. Duan, J. et al. Planar refraction and lensing of highly confined polaritons in anisotropic media. *Nat. Commun.* **12**, 4325 (2021).
69. Álvarez-Pérez, G. et al. Negative reflection of nanoscale-confined polaritons in a low-loss natural medium. *Sci. Adv.* **8**, eabp8486 (2022).
70. Tudi, A., Han, S., Yang, Z. & Pan, S. Potential optical functional crystals with large birefringence: recent advances and future prospects. *Coordin. Chem. Rev.* **459**, 214380 (2022).
71. Fali, A. et al. Refractive index-based control of hyperbolic phonon-polariton propagation. *Nano Lett.* **19**, 7725–7734 (2019).
72. Folland, T. G. et al. Reconfigurable infrared hyperbolic metasurfaces using phase change materials. *Nat. Commun.* **9**, 4371 (2018).

[1]CAS Key Laboratory of Nanophotonic Materials and Devices, CAS Key Laboratory of Standardization and Measurement for Nanotechnology, National Center for Nanoscience and Technology, Beijing, People's Republic of China. [2]Center of Materials Science and Optoelectronics Engineering, University of Chinese Academy of Sciences, Beijing, People's Republic of China. [3]School of Materials Science and Engineering, Shanghai Jiao Tong University, Shanghai, People's Republic of China. [4]ICFO—Institut de Ciencies Fotoniques, The Barcelona Institute of Science and Technology, Castelldefels (Barcelona), Spain. [5]ICREA—Institució Catalana de Recerca i Estudis Avançats, Barcelona, Spain. [6]CIC nanoGUNE, Donostia-San Sebastián, Spain. [7]CIC nanoGUNE BRTA and Department of Electricity and Electronics, UPV/EHU, Donostia-San Sebastián, Spain. [8]IKERBASQUE, Basque Foundation for Science, Bilbao, Spain. [9]These authors contributed equally: Na Chen, Hanchao Teng. ✉e-mail: huh@nanoctr.cn; r.hillenbrand@nanogune.eu; daiqing@sjtu.edu.cn

Methods

Nanofabrication of the devices

Square holes (50 μm × 50 μm) were patterned on a 300-nm SiO_2/500-μm Si substrate using 100-kV electron-beam lithography (Vistec 5000+ES) on approximately 350 nm of ZEP520A electron-beam lithography resist. The patterns were subsequently transferred to the substrate via reactive ion etching (RIE) using C_4F_8 and SF_6 gases (SENTECH, Etchlab 200). Then, the substrate was immersed in hot butanone at 80 °C for 25 min and subjected to a gentle rinse of isopropanol for 3 min to remove the resist layer, followed by nitrogen-gas drying and thermal baking. The remaining residues on the SiO_2 surface were further removed by oxygen plasma cleaning with 5 Pa and 80 W for 10 min (ref. 73).

Single-crystalline Au flakes, grown on glass coverslips by the thermolysis method[63], were transferred onto the patterned substrate through a deterministic dry-transfer process using a polydimethylsiloxane stamp. A rotation stage under an optical microscopy enabled precise alignment of the Au edge with the square-hole boundary, thereby forming a well-defined Au–air boundary. The α-MoO_3 flakes (Shanghai Onway Technology) were mechanically exfoliated from bulk crystals and subsequently transferred onto the aforementioned Au–air hybrid substrate, covering both the Au flake and the square holes.

Two antenna geometries (length × width × thickness: 3 μm × 250 nm × 50 nm and 3 μm × 3 μm × 50 nm) were patterned on different samples to fulfill distinct excitation purposes, using the same electron-beam lithography system with ~350 nm of PMMA950K resist. After that, electron-beam evaporation was used to deposit 5-nm Ti and 50-nm Au in a vacuum chamber at a pressure of $<5 \times 10^{-6}$ torr to fabricate the Au antennas. The lift-off process was carried out by immersing the samples in a hot acetone bath at 80 °C for 25 min, followed by rinsing with isopropanol for 3 min, nitrogen-gas drying, and thermal baking.

Near-field optical microscopy measurements

An s-SNOM setup (Neaspec) equipped with a tunable quantum cascade laser (890–2,000 cm^{-1}) was utilized for near-field measurements using atomic force microscopy tips coated with Pt and an apex radius of ~25 nm (NanoWorld). A tapping frequency and tapping amplitude of ~270 kHz and ~30–50 nm, respectively, was used. The tip was illuminated with a *p*-polarized mid-infrared beam focused to a spot with a lateral size of ~25 μm, which also illuminated the antennas. Demodulation of the detector signal at the third harmonic of the tapping frequency (S_3) provided near-field amplitude and phase images with effective suppression of background signals. In this study, we present and analyze the near-field amplitude (S_3) images[74].

Calculation of dispersion and IFCs of phonon polaritons

The transfer matrix method was employed to calculate the dispersion and IFCs of different-order phonon polaritons in α-MoO_3. The system was modelled as a two-dimensional waveguide consisting of three stacked layers: a cover layer (air), an intermediate layer (α-MoO_3) and a substrate (Au or air). In this analysis, air and Au were described by isotropic dielectric tensors, whereas the α-MoO_3 layer was treated as anisotropic.

Calculation of excitation efficiency for polaritons with different orders by dyadic Green's function theory

The antenna was simplified to an oscillating dipole along the *x* direction, placed at a height of $z_0 = 30$ nm on the surface, which was used to mimic the excitation of the antenna. In this case, the electric field distribution E_z^p along the *z* direction can be expressed as $E_z^p = \alpha_{zx} p_x$, where $\alpha_{zx} = \frac{ik_x \alpha_{ant}}{2\varepsilon}(e^{ik_z|z-z_0|} + r^p(k_x, k_y)\, e^{ik_z(z+z_0)})$ denotes an electric field of dipole p_x. α_{ant} is the strength of the dipole, which can be calculated using COMSOL Multiphysics and $r^p(k_x, k_y)$ is the reflection coefficient of different layers. Further considering the tip as the collector of polaritons that oscillate along the *z* axis, we get $z_d(t) = b + \delta z(1 - \cos\Omega t)$, where $b = 60$ nm is the distance between the tip apex and the surface and $\delta z = 130$ nm is the tapping amplitude of the tip and $\Omega = 270$ kHz is the tapping frequency. Considering the averaged time, we can define the surface excitation efficiency $\langle \alpha_z \rangle_t$ of the system (Supplementary Note 1) as

$$\langle \alpha_z \rangle_t = \frac{1}{T} \int \frac{ik_x \alpha_{ant}}{2\varepsilon} e^{ik_z(z_d + z_0)} dt, \quad (2)$$

where z_0 is the point dipole position above the surface, ε represents the dielectric function of the surrounding environment and T is the period of tip tapping.

Electromagnetic simulations

A finite element method software (COMSOL Multiphysics v. 5.5) was used to simulate the electromagnetic field. The model was constructed by following the geometrical specifications in the experimental samples. Perfectly matched layers were set up at all boundaries around the model to reduce reflections. The incident light was set as a *p*-polarized plane wave with an angle of 45° to the surface. The electric field distribution was calculated on a plane situated 20 nm above the uppermost surface of the sample.

Data availability

The data that support the findings of this study are available in the Article and the Supplementary Information. Source data are provided with this paper.

References

73. Hu, H. et al. Active control of micrometer plasmon propagation in suspended graphene. *Nat. Commun.* **13**, 1465 (2022).
74. Ocelic, N., Huber, A. & Hillenbrand, R. Pseudoheterodyne detection for background-free near-field spectroscopy. *Appl. Phys. Lett.* **89**, 101124 (2006).

Acknowledgements

We acknowledge D. N. Basov (Columbia University) for valuable discussions and are grateful to X. Xi and X. Wang (State Key Laboratory of New Ceramics & Fine Processing, Tsinghua University) for scanning near-field optical microscopy measurements. The work was financially supported by the National Natural Science Foundation of China (grant numbers 52322209, 52172139 and 52350314 to H.H.), the National Key Research and Development Program of China (grant number 2021YFA1201500, to Q.D.), Beijing Nova Program (grant numbers 2022012 and 20240484600 to H.H.), Youth Innovation Promotion Association of Chinese Academy of Sciences (grant number 2022037 to H.H.), and the Postdoctoral Fellowship Program and China Postdoctoral Science Foundation (grant numbers BX20250181 and 2024M760685, to N.C.). R.H. acknowledges grant number CEX2020-001038-M funded by the Spanish MICIU/AEI/10.13039/501100011033 and grant number PID2021-123949OB-I00 funded by the Spanish MICIU/AEI/10.13039/501100011033 and ERDF/EU. F.J.G.A. acknowledges the ERC (grant number 789104-eNANO) and the Spanish MICINN (grant numbers PID2020-112625GB-I00 and SEV2015-0522).

Author contributions

Q.D., R.H. and H.H. conceived the idea. Q.D., R.H. and F.J.G.A. supervised the project. N.C. and H.H. prepared the samples and conducted the near-field measurements. H.T. and F.J.G.A. developed the theoretical framework and performed the simulations. All authors contributed to the data analysis and discussion of the results. H.H., N.C. and H.T. co-wrote the manuscript with input and feedback from Q.D., R.H. and F.J.G.A.

Competing interests

R.H. is a co-founder of Neaspec GmbH, now part of attocube systems GmbH, a company that manufactures s-SNOM systems, including the one used in this study. The remaining authors declare no competing interests.

Correspondence and requests for materials should be addressed to Hai Hu, Rainer Hillenbrand or Qing Dai.